ROYAL SOCIETY OF CHEMISTRY

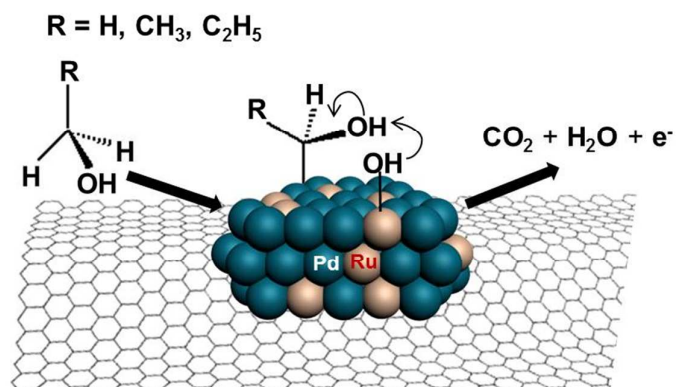Journal of
Materials Chemistry A

The binary PdM catalysts (M=Ru, Sn, or Ir) over reduced graphene oxide support for electro-oxidation of primary alcohols (methanol, ethanol, 1-propanol) in alkaline condition

SCHOLARONE™
Manuscripts

Table of Contents

Journal Name

ARTICLE

The binary PdM catalysts (M=Ru, Sn, or Ir) over reduced graphene oxide support for electro-oxidation of primary alcohols (methanol, ethanol, 1-propanol) in alkaline condition

Eun Ja Lim,[ab] Youngmin Kim,[ab] Sung Mook Choi,[c] Seonhwa Lee,[bd] Yuseong Noh,[ab] and Won Bae Kim[*abd]

High metal loaded (60 wt. %) binary PdM (M=Ru, Sn, Ir) catalysts were synthesized on reduced graphene oxide (RGO) using borohydride reduction method, and they were used for electro-oxidations of simple alcohols, such as methanol, ethanol, and 1-propanol, in alkaline media. Cyclic voltammetry (CV) tests indicated that the Pd-based binary systems could improve electrochemical activities significantly compared to the monometallic Pd/RGO catalyst. Among the prepared catalysts, addition of Ru into Pd (PdRu/RGO) resulted in remarkably improved electrocatalytic activity in terms of larger peak current densities and lower onset potential in all electro-oxidation cases with methanol, ethanol, and 1-propanol. CO-stripping tests also revealed that the onset and peak potentials for the CO oxidation appear to decrease by the addition of Ru to the Pd/RGO, indicating that the electro-oxidation of CO can take place more efficiently on the PdRu/RGO catalyst with assistance of easily formed hydroxyl groups. Such improvement of electrocatalytic performance can be ascribed to structural and chemical modifications of the Pd catalysts. Physicochemical properties of the PdM/RGO catalysts were characterized by X-ray diffraction (XRD), transmission electron microscopy (TEM), X-ray photoelectron spectroscopy (XPS), and X-ray absorption spectroscopy (XAS).

Introduction

Direct alcohol fuel cells (DAFCs) have attracted much attention as one of the promising electric power generation systems due to the use of various liquid fuels such as methanol, ethanol, 1-propanol.[1-3] Liquid fuels are easily handled, stored and transported in comparison with other gaseous fuels which need complicated systems for storage[4] and external fuel reforming.[5] In general, the overall electro-oxidation of aliphatic alcohols over Pt-based catalysts can be represented as below[6]:

$$C_nH_{2n+1}OH + (2n-1)H_2O \rightarrow nCO_2 + 6nH^+ + 6ne^-$$
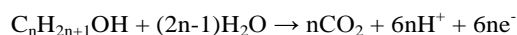
The electro-oxidation of methanol takes place on active metal catalysts like Pt through adsorption and decomposition with oxidant species such as OH.[7] The oxidation processes of ethanol and 1-propanol are rather complicated compared to that of methanol, because of the presence of more C-H bonds as well as C-C bonds that are generally known to be more difficult

to break.[1,8] During oxidation of alcohols, several byproducts and poisoning species (for example, CO) are produced and easily adsorbed on the active site of the Pt-based catalysts[9], thereby reducing turnover rate for the catalytic oxidation reaction of alcohol molecules. Therefore, development of active and stable catalysts for promoting the electro-oxidation reactions of methanol, ethanol, and 1-propanol is required for applications of DAFCs.

Most research for the DAFCs has focused on acid electrolyte systems,[10] where Pt-based catalysts, which are costly with a limited supply, are only options as the active and stable electrocatalysts in such acidic condition[11]. However, in high pH conditions, some non-Pt catalysts such as silver, nickel, and palladium can be employed as the active electrocatalysts which could facilitate the cathodic oxygen reduction reaction and the anodic oxidation reactions, making the alkaline based fuel cells to be promising.[12] Among the non-Pt catalysts, Pd-based catalysts show good performance with resistance to CO poisoning and comparable activity to the Pt catalysts for the

electro-oxidations of ethanol and methanol under the alkaline condition.[2,13] However, bare Pd has unsatisfactory capability for C-H and C-C bond cleavage and it is easily poisoned by CO or carbonaceous intermediates.[14] In this regard, combination of other metal or metal oxide[15,16] with Pd is promising approach to modify the structural, physical, and electronic properties of Pd, which can give rise to the electronic[17-19] and bifunctional effects.[20,21] Second metal or metal oxide could change the electron property of Pd and facilitate the formation of OH_{ads} species at lower potentials, which plays key roles in minimizing the effect of CO poisoning. There are several reports that the Pd-based bimetallic catalysts (e.g., PdNi, PdAu, PdY, PdPb, PdAg) have better performance than the monometallic Pd catalysts.[22-26]

In this work, the electrocatalytic performances of binary PdM (M = Ru, Sn, Ir) are explored for the electro-oxidations of primary alcohols (e.g., methanol, ethanol, and 1-propanol) in alkaline media. The reduced graphene oxide (RGO) is used as an efficient support to accommodate highly dispersed PdM nanoparticle catalysts, which were prepared using $NaBH_4$ reduction method combined with freeze-drying procedure. In this method, uniform and well dispersed nanoparticles can be synthesized even with a high metal loading over the RGO support with excellent physicochemical properties of graphene such as large surface area (theoretically, ca. 2630 m^2g^{-1}),[27] good chemical stability,[28] and excellent electrical conductivity.[29] The relationship between physicochemical properties and electrocatalytic activities will be explored and discussed with respect to the second metal elements for the electro-oxidations of primary alcohols such as methanol, ethanol, and 1-propanol.

Experimental Section

Chemicals.
Palladium(II) nitrate hydrate ($Pd(NO_3)_2 \cdot nH_2O$, Sigma-Aldrich), ruthenium(III) chloride hydrate ($RuCl_3 \cdot nH_2O$, Sigma-Aldrich), tin(II) chloride dihydrate ($SnCl_2 \cdot 2H_2O$, Sigma-Aldrich), iridium(III) chloride hydrate ($IrCl_3 \cdot nH_2O$, Sigma-Aldrich), sodium borohydride ($NaBH_4$, Sigma-Aldrich), deionized water (DI water, 18 MΩ•cm, Millipore), graphite (Carbonix, Korea), methanol (HPLC grade, Fischer Scientific Korea), and ethanol (HPLC grade, Fischer Scientific Korea), 1-propanol (ACS reagent, Sigma-Aldrich) were purchased from the specified suppliers and were used as received without further purification.

Synthesis of Ru, Sn or Ir-modified Pd catalysts over RGO.
The natural graphite was pre-oxidized in an oxidizing solution containing H_2SO_4, $K_2S_2O_8$, and P_2O_5, as described in according to our previous report[30] and the pre-oxidized graphite was further oxidized to graphite oxide according to the Hummer's method reported in the literature[31]. The prepared graphite oxide was ultrasonicated in distilled water (DI) to subsequently produce exfoliated graphene oxide (GO) nanosheets. Reduced graphene oxide (RGO)-supported binary Pd-based catalysts of PdRu, PdSn, and PdIr were prepared by one-pot reduction process using sodium borohydride for the reduction of both the

metal precursors and the graphene oxide (GO) supports. The elemental ratio of Pd to the second metal (Ru, Sn, Ir) was fixed to 9:1 with 60 wt. % Pd metal loading. A precalculated amount of Pd salt ($Pd(NO_3)_2 \cdot nH_2O$) with Ru salt ($RuCl_3 \cdot nH_2O$), Sn salt ($SnCl_2 \cdot nH_2O$), or Ir salt ($IrCl_3 \cdot nH_2O$) for the binary Pd-based catalysts of PdRu, PdSn, and PdIr, respectively, was added and completely dissolved in the graphene oxide-suspended solution with vigorous stirring. Subsequently, 0.01 M $NaBH_4$ was added drop by drop into the stirred solution for 1.5 h using a syringe pump (KD Scientific Inc.) to reduce both the metal ions and GO. The resulting slurries were centrifuged and washed thoroughly with DI water, and subsequently vacuum dried via a freeze-drying method. Actual metal loading and elemental compositions of binary Pd-based catalysts/RGO were identified using ICP-MS analyses and the surface composition was examined by XPS.

Physicochemical characterizations of PdM/RGO catalysts.
The catalyst phases and alloy formation with respect to the second metals in the prepared samples were identified using X-ray diffraction (XRD, Rigaku Rotalflex) with Cu Kα (λ = 1.5401 Å) source with a Ni filter. The source was operated at 40 kV and 100 mA, and the 2θ angular region between 10° and 80° was explored at a scan rate of 1° min^{-1}. The crystallite size and lattice parameter of the Pd-based nanoparticle catalysts were calculated from the Pd (111) diffraction peak fitted using the Gaussian function.

The morphologies of Pd and binary PdM (M= Ru, Ir, Sn) nanoparticles on the RGO support were investigated using transmission electron microscope (TEM) operated at 300 kV. All TEM samples were prepared by ultrasonically dispersing the catalyst particles in an ethanol solution. Drops of the suspension were deposited onto a standard Cu grid (200-mesh) covered with a carbon film and dried for 1 h to allow ethanol to be evaporated, leaving the catalyst particles dispersed on the grid prior to being inserted into the microscope. More than 130 different particles visible on the micrographs were employed to estimate average particle size of the catalysts. To elucidate the purity and chemical composition of the Pd alloy nanoparticles, energy dispersive X-ray spectroscopy (EDS) analysis was also performed at 300 kV using a Technai G2 F30 S-Twin attached to the TEM.

The surface compositions and chemical states of the samples were analyzed by X-ray photoelectron spectroscopy (XPS, Multilab 2000, VG, UK) with a non-monochromatic Al K_α X-ray source (E = 1486.6 eV). The sample powders were attached to the sample holder using a small piece of carbon tape. No significant charging effects were detected. Data processing was performed using the XPSPEAK software program. The background was corrected using the Shirley method, and the binding energy (BE) of the C 1s peak from the support at 284.5 eV was used as an internal standard. The surface atomic ratios of second metal to Pd were calculated from peaks areas normalized by atomic sensitivity factor of the corresponding element.[32] Peak areas were estimated by calculating the integral of each peak after subtracting a Shirley background and fitting

the experimental peak by a combination of Lorenzian/Gaussian (L/G) curves of a variable proportion.

X-ray absorption measurements were carried out on the 7D beamline of the Pohang Accelerator Laboratory (PLS-II, 3.0 GeV, Korea) using a Si (111) double crystal monochromator to monochromatize the X-ray photon energy. The spectra were taken at room temperature in a transmission mode for the K-edge of Pd (24.350 keV) under the ambient condition and calibrated using a standard Pd metal foil. The X-ray absorption near edge structure (XANES) and extended X-ray absorption fine structure (EXAFS) data were analyzed with the IFEFFIT software package (ATHENA and ARTEMIS program).[33] The pre-edge background was removed through fitting a pre-edge region with a straight line and subtracting the extrapolated values from the entire spectrum. The resulting elemental absorption $\mu(E)$ was then normalized by using atomic-like absorption $\mu_0(E)$ at the edge. The data from Pd K-edges for bimetallic Pd-M/RGO catalysts and Pd/RGO were fitted in R space. The theoretical standard for Pd-Pd single scattering was calculated with the FEFF code 6.01 using the structural information for Pd metal.[34] The parameter of amplitude reduction factors (S_0^2) was set to the values of 0.804 (Pd K-edge) determined from fitting the corresponding metal foil. Only the k range of 3–13 Å^{-1} and the R range of 1.8–3.1 Å were fitted on k^3 weighted EXAFS data with the first-shell single scattering paths.

Electrochemical measurements.

Electrocatalytic activities toward alcohol oxidations were performed in a three-electrode cell by cyclic voltammetry (CV) measurements using a Solartron Analytical instrument (AMET-EK model 1400). A Pt wire and Hg/HgO (MMO) were used as counter and reference electrode, respectively. The measured potentials versus the MMO reference electrode were converted to the reversible hydrogen electrode (RHE) scale via the Nernst equation.[35] A glassy carbon (GC, with geometric area of ca. 0.196 cm^2), as a working electrode (WE), was carefully cleaned by polishing with 1, 0.3, and 0.05 µm Al$_2$O$_3$ pastes until a mirror-like surface was obtained. For the catalysts mounting on the WE, 20 µl of the catalyst ink suspended homogeneously in 2 ml of ethanol solution that contained 3.5 µl of Nafion® ionomer solution (in 5 wt. % solution from Sigma-Aldrich) were pipetted out on top of the GC to yield a metal loading of 0.1 mg cm^{-2} and dried in an oven at 343 K for 20 min. Electrochemical tests were carried out in the prepared solutions after degassing oxygen by pure N$_2$. The CV tests were performed within the potential range of -0.9 to 0.5 V (vs. MMO) at a scan rate of 50 mVs^{-1} in the 1.0 M NaOH solutions that contain 1.0 M individual alcohols (methanol, ethanol, and 1-propanol), respectively.

Results and discussion

Figure 1 shows representative TEM images of the Pd/RGO and PdM/RGO (M = Ru, Sn, and Ir) catalysts. Because GO support has very thin and flexible two-dimensional sheet-like
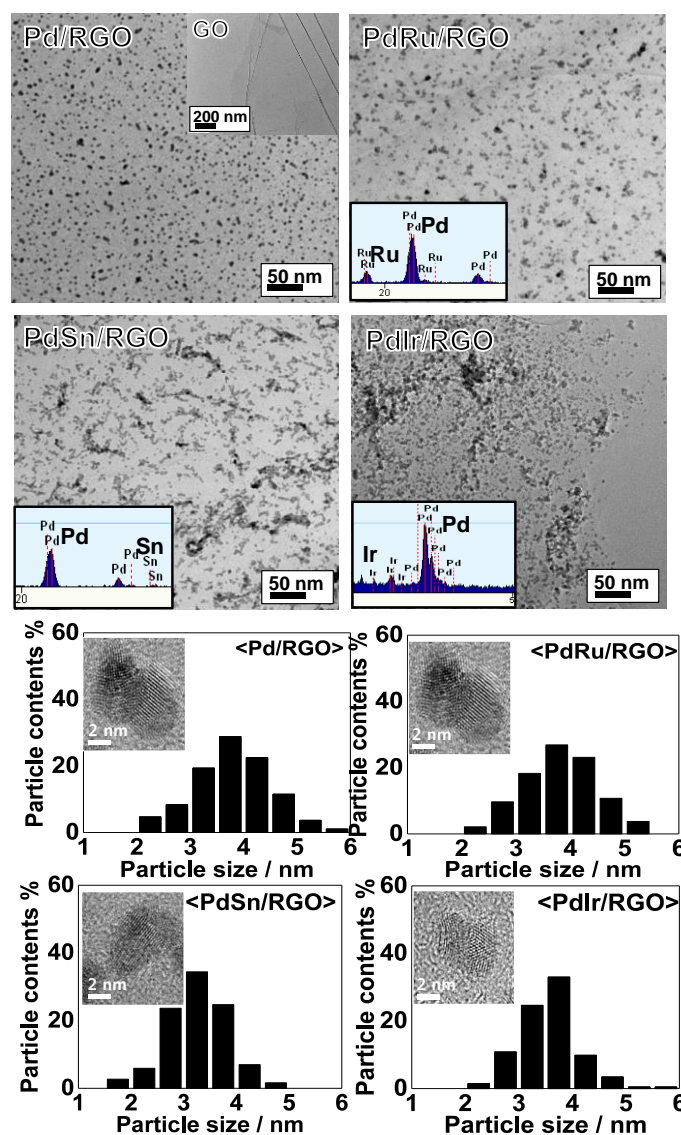

Figure 1. Representative TEM images of Pd/RGO (inset shows SEM image of GO), PdSn/RGO, PdRu/RGO, PdIr/RGO catalysts together with EDS spectrum (inset) and particle-size distributions of the catalyst nanoparticles (inset shows HR-TEM image of Pd, PdSn, PdRu, and PdIr particle on RGO).

morphology as shown in the inset of Figure 1, which can act as excellent support material to accommodate highly concentrated metal nanoparticles, uniform and well dispersed Pd-based nanoparticles can be seen on the RGO support for all of the synthesized catalysts. The individual particles of Pd, PdRu, PdSn, and PdIr reveal the spherical shape with sizes of 3.3–3.8 nm, as can be seen in the HR-TEM images in the inset images of Figure 1. The sizes of the Pd-based nanoparticles were estimated by averaging the diameter of 150 nanoparticles chosen in the TEM images. The mean particle diameter, d, is calculated from following equation:

$$d = \sum n_i d_i / \sum n_i$$

where n_i is the frequency of the catalyst particles having diameter of size d_i. The particle size distributions indicate that the nanoparticle catalysts have similar metal particle sizes of 3.3–3.8 nm. These values are consistent with those observed from XRD in Figure 2 by the full width half maxi- mum (FWHM) method at the Gaussian-fitted Pd (111) peaks using the Scherrer's equation,[36] exhibiting the mean crystallite sizes of *ca.* 4.0, 4.3, 3.9, and 4.0 nm for the Pd/RGO, PdRu/RGO, PdSn/RGO, and PdIr/RGO, respectively, as summarized in Table 1. These results from TEM and XRD indicate that the NaBH₄ reduction method in low temperature condition is efficient to prepare highly dispersed Pd-based binary catalysts even with 60 wt. % of metal loading. Negligible difference in metal particle sizes in our prepared catalysts allows the particle size effect to be excluded from the influential parameters for the electro-catalytic activity of the electro-oxidation of alcohols.

The inset figures of point-resolved EDS analysis revealed the purity and chemical composition of the nanoparticles loaded on the RGO for the prepared catalysts. The atomic compositions were approximately 9:1 of Pd:M, which is in good agreement with the nominal value calculated from the added amounts at its preparation step, indicating complete reduction of salts was achieved under these conditions.

Table 1. Structural parameters of the Pd/RGO, PdRu/RGO, PdSn/RGO, and PdIr/RGO catalysts characterized by XRD and TEM analyses.

Catalyst	Particle size (nm) TEM[a]	Crystallite size (nm) XRD[b]	2θmax[c] (°) (111)	Lattice parameter[d] (Å)
Pd/RGO	3.8 nm ± 0.74	4.0	39.54	3.94
PdRu/RGO	3.8 nm ± 0.68	4.3	39.83	3.91
PdSn/RGO	3.3 nm ± 0.57	3.9	39.45	3.95
PdIr/RGO	3.6 nm ± 0.52	4.0	39.58	3.93

[a] Mean particle diameter of the Pd-based catalysts from TEM images using at least 150 visible particles.
[b] Crystallite sizes of the Pd-based catalysts calculated by line broadening of power XRD peaks.
[c] The angular position of Pd(111) reflection peak.
[d] Lattice parameter calculated from XRD analysis.

Figure 2 (upper figure) shows XRD patterns of the binary Pd-based catalysts of PdRu, PdSn, and PdIr that were supported on the RGO nanosheets, indicating the information on the crystallographic structures of the metal catalysts. It could be clearly seen that the prepared catalysts display the typical characteristic peaks of face cantered cubic (*fcc*) Pd phase from (111), (200), (220) planes at around 39.7°, 46.0°, 66.6°, respectively. There were no noticeable separation peaks from the metallic phases of Ru, Sn, and Ir or their oxide phases, which indicate a good degree of alloying between Pd and the second metals. Comparing the enlarged Pd (111) peak region as shown in Figure 2 (lower figure), diffraction peak position of the Pd (111) seems to be slightly shifted to higher 2θ values in

the PdRu/RGO and PdIr/RGO compared to that of Pd/RGO, which could clarify the alloy formation between Pd and the second element (Ru or Ir) by incorporation of Ru or Ir element to the *fcc* structure of Pd. In contrast, introduction of Sn to the Pd appears to cause the shift of Pd (111) peak toward lower 2θ values. Lattice parameter changes of all the catalysts listed in Table 1, reflecting the formation of alloying, were also evaluated using the angular position ($2\theta_{max}$) of the (111) peak from Figure 2. The lattice parameter of 3.94 Å for the Pd/RGO catalyst in this work is in a good agreement with that of nano-size Pd particle reported in elsewhere.[37] Lattice parameter change could be resulted from the structural distortion of Pd nanoparticles due to the partial substitution of Pd by the second element which has different atomic sizes from Pd. Atomic radius of metals is in order of Ru (R_{Ru}= 1.34 Å) < Ir (R_{Ir}=1.36 Å) < Pd (R_{Pd}= 1.37 Å) < Sn (R_{Sn}= 1.40 Å), thus size mismatch between the Pd and the second metals generally induces contraction or expansion of lattice parameter of the host Pd metal.[36] The lattice parameter of Pd in the PdSn/RGO catalyst shows a slightly increased value as compared to the monometallic Pd/RGO. On the contrary, in cases of incorporation of Ru or Ir with smaller atomic sizes than the Pd,[38,39] the lattice contraction of Pd crystal structure could happen on the PdRu/RGO and PdIr/RGO catalysts.
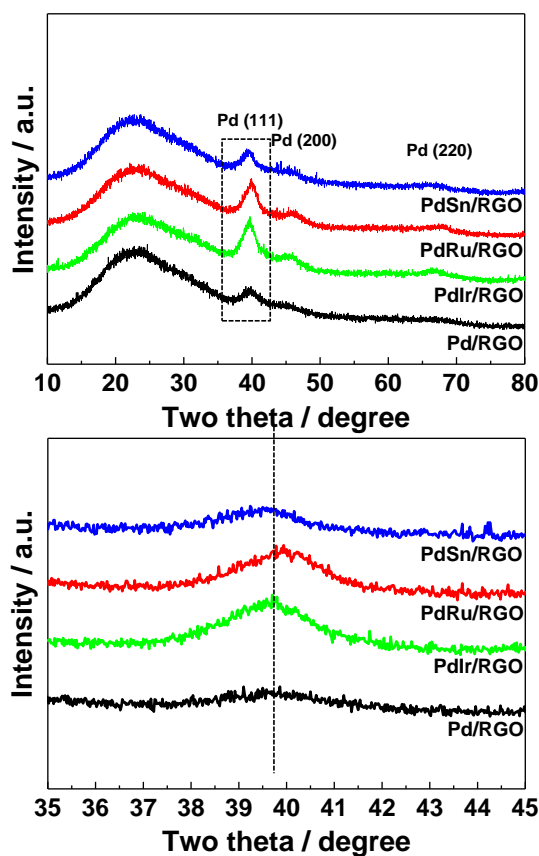

Figure 2. X-ray diffraction patterns of the prepared PdSn/RGO, PdRu/RGO, PdIr/RGO, and Pd/RGO catalysts obtained in the scan range 10-80° (upper figure) and the selected scan range in the vicinity of Pd (111) reflection peaks (lower figure).

In order to investigate the electronic structure and surface composition of the prepared catalysts, XPS analyses were carried out. Figure 3 shows the Pd(3d), Ru(3p), Sn(3d), and Ir(4f) regions in the XPS spectra of Pd/RGO, PdRu/RGO, PdSn/RGO, and PdIr/RGO catalysts. The Pd 3d spectrum consists of two spin-orbit splitting peaks of Pd $3d_{5/2}$ and Pd $3d_{3/2}$ states. Each peak was deconvoluted with different Pd oxidation states of metallic Pd and PdO. The binding energy of core-level Pd $3d_{5/2}$ electrons and the relative percentage of each oxidation states for Pd are summarized in Table 2. The percentages of the metallic state and oxidized Pd species were calculated on the basis of the integration of their individual components. It was found that the metallic Pd species were pre-

Table 2. Electronic parameters of the Pd/RGO, PdRu/RGO, PdSn/RGO, and PdIr/RGO catalysts characterized by XPS and XANES analyses.

Catalyst	Binding energy (eV)		M/Pd[b]	XANES	
	Pd $3d_{5/2}$	Ru 3p, Sn 3d, Ir 4f		E_0 (eV)[c]	WL intensity (a.u.)[d]
Pd/RGO	335.7(68)[a] 336.8(32)[a]		-	24350.9	0.958
PdRu/RGO	335.7 (62) 337.0 (38)	462.5 (81) 465.8 (19)	0.38	24350.4	0.956
PdSn/RGO	335.6 (59) 336.7 (41)	486.4 494.8	0.25	24352.3	0.960
PdIr/RGO	335.9 (67) 337.3 (33)	61.4 64.5	0.16	24352.2	0.961
Pd foil	-	-	-	24351.7	0.943

[a]Relative peak area (%) of the Pd^0 and Pd^{2+} species.
[b]Surface M/Pd atomic ratio calculated from XPS by using peak area normalized on the basis of atomic sensitive factors.
[c]Pd K-edge energy.
[d]WL (White line) intensity.

dominantly present with about 60 % in the prepared catalysts. The oxidized Pd species with about 40 % was present, which might be produced on the catalyst surface through passivation process during the sample preparation. Surface composition ratio of the second metal to Pd (M/Pd) was evaluated by using peak areas normalized on the basis of atomic sensitive factors (see Table 2). The PdRu/RGO catalyst shows a higher M/Pd ratio of 0.38 as compared to the experimentally added ratio of 0.1, suggesting that there might be a significant surface Ru enrichment by segregation of Ru onto the surface due to the smallest atomic radius.[40] As shown in Figure 3, the XPS spectrum of Ru(3p) from the PdRu/RGO catalyst was analyzed instead of Ru(3d) due to the overlapping peaks between C(1s) and Ru(3d). The Ru $3p_{3/2}$ spectrum was deconvoluted into two distinguishable peaks of different intensities, which correspond to metallic Ru and RuO_2.[41] Two peaks of Ir(4f) spectra ($4f_{5/2}$, $4f_{7/2}$) are located at binding energy of 61.4 and 64.5 eV,
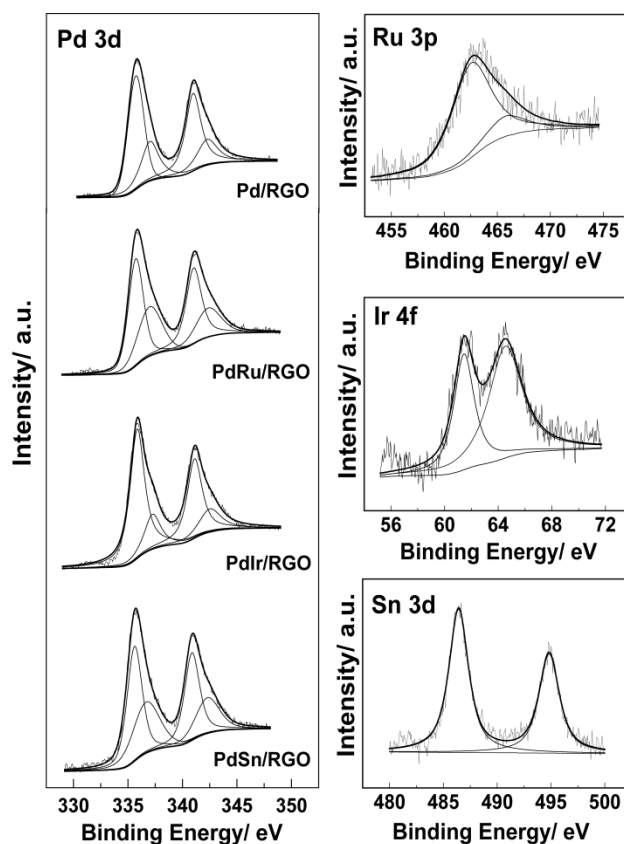

Figure 3. X-ray photoelectron spectra of Pd 3d, Ru 3p, Ir 4f, and Sn 3d for the Pd/RGO, PdRu/RGO, PdIr/RGO, and PdSn/RGO catalysts.

respectively, as shown in Figure 3.[42] The spectra of Sn $3d_{5/2}$ and Sn $3d_{3/2}$ from the spin-orbital splitting were observed at 61.4 and 64.5 eV, respectively.[43]

Electronic structure of Pd/RGO and binary PdM/RGO system was investigated by XANES spectra recorded at the Pd K-edge as shown in Figure 4 and summarized in Table 2. The absorbance spectra at the Pd K-edge (24350 eV) are assigned to the electron transition from 1s to 4d states. The overall XANES spectra for the Pd/RGO and binary PdM/RGO are similar to that of the Pd foil except the peak intensity after the edge absorption. The white line (WL), which is a strong peak above the edge energy position and frequently recognized as an important parameter in the catalytic activity,[44] is associated with the density of vacant 4d electronic states in Pd. The white line magnitudes of Pd K-edges for the prepared PdM/RGO and Pd/RGO catalysts were higher than that of Pd metal foil (see the inset of Figure 4 and Table 2). The intensity of the Pd WL appeared to increase in the order of PdRu/RGO < Pd/RGO < PdSn/RGO < PdIr/RGO. The decreased WL intensity for the PdRu/RGO could be caused by the electron donation from the adjacent Ru to the Pd, resulting in partial filling of the unoccupied Pd 4d orbitals.[45] On the contrary, the WL intensities appeared to be higher in the cases of PdSn/RGO and PdIr/RGO, implying a less filled d band state of Pd in the catalysts.

EXAFS data were collected to further characterize the structural

Table 3. EXAFS fitting results of Pd K-edge for the first shell of Pd/RGO, PdRu/RGO, PdSn/RGO, and PdIr/RGO catalysts.

Catalyst	Shell	N^a	R (Å)^b	ΔE (eV)^c	σ^2 (Å ^{2})^d	R-factor
Pd foil	Pd-Pd	12	2.743±0.002	0.5±0.6	0.0056±0.0003	0.0019
Pd/RGO	Pd-Pd	7.03±0.33	2.743±0.002	-0.7±0.4	0.0079±0.0003	0.0012
PdRu/RGO	Pd-Pd	7.04±1.21	2.734±0.010	1.1±0.8	0.0065±0.0007	0.0009
	Pd-Ru	1.37±1.14	2.840±0.044			
PdSn/RGO	Pd-Pd	6.93±2.33	2.746±0.018	-0.6±2.6	0.0073±0.0020	0.0036
	Pd-Sn	0.59±1.59	2.858±0.219			
PdIr/RGO	Pd-Pd	6.43±0.32	2.743±0.002	-1.6±0.4	0.0076±0.0003	0.0004
	Pd-Ir	0.83±0.27	2.715±0.019			

^{a}The average coordination number for the coordination shell. ^{b}Interatomic distance. ^{c}E$_0$ shift of the path. ^{d}Debye-Waller factor.

states of palladium in the RGO-supported binary PdM catalysts. Figure 5 shows the phase-uncorrected radial structural functions (RSFs) obtained by Fourier transformation (FT) of EXAFS spectra at the Pd K-edge for the Pd/RGO and PdM/RGO catalysts together with Pd foil reference. The main peaks appearing between *ca.* 2 and 3 Å in the RSFs correspond to Pd-Pd and Pd-M interatomic distances shifted from their true positions by a phase shift, and their intensities are closely associated with the average coordination number.[46] In order to obtain quantitative information on the coordination number (CN) and radial distance of the local environment of Pd, we curve-fitted the experimentally derived RSF with theoretical Pd-Pd and Pd-M scatterings and the fitting results are listed in Table 3. The CN of Pd/RGO exhibited about 7, which is smaller than the theoretical value (CN = 12) of bulk Pd foil. Small particle size with increased fraction of surface sites is responsible for this small CN of the Pd nanoparticles. Similarly, for the binary PdM/RGO catalysts, the total CN contributed by both Pd-Pd and Pd-M interactions was in the range of 7.0–8.4. The Pd-Pd bond distances of PdRu/RGO, PdIr/RGO, Pd/RGO, and PdSn/RGO were determined to be 2.734±0.002, 2.743±0.002, 2.743±0.002, and 2.746±0.018, respectively. Contraction and expansion for the Pd-Pd bond distance in the alloys were observed, which are in good agreement with the XRD results.

The Pd-based binary catalysts synthesized on the graphene supports were employed as the electro-oxidation catalysts for methanol, ethanol, and 1- propanol in alkaline media. Figure 6 presents typical CV curves of the Pd/RGO, PdRu/RGO, PdSn/RGO, and PdIr/RGO catalysts which were conducted in 0.1 M NaOH electrolyte. It can be observed that OH adsorption and reduction of oxygen layer on PdO species appear similarly on the binary catalysts of PdRu, PdSn, and PdIr/RGO during anodic and cathodic sweeps. Due to the difficulty in definition of the hydrogen adsorption/desorption regions over the Pd surface,[47,48] electroactive surface (EAS) was estimated from the cathodic peak of PdO associated with reduction charges of the surface PdO species (405 μCcm^{-2})[48] at the fully activated CV
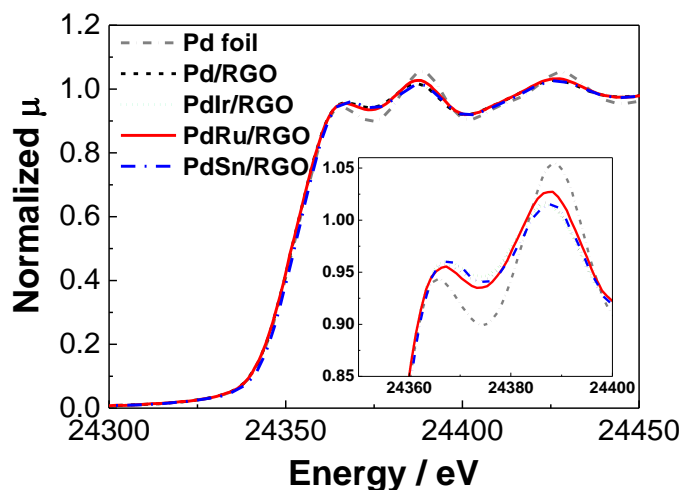

Figure 4. Pd K-edge XANES spectra for the Pd/RGO, PdRu/RGO, PdIr/RGO, and PdSn/RGO catalysts together with Pd foil as the reference.

curve. The EAS values of Pd/RGO, PdRu/RGO, PdSn/RGO, and PdIr/RGO calculated from the coulombic charge for PdO reductions were 58.1, 52.0, and 64.9, 61.6 m^{2}g^{-1}, respectively, which are in line with other reports for the Pd-based nanoparticles on graphene supports.[47,48]

The electrocatalytic activity of the Pd/RGO, PdRu/RGO, PdSn/RGO, and PdIr/RGO was investigated by performing CV tests in 1.0 M NaOH with 1.0 M of individual alcohols (methanol, ethanol, and 1-propanol) at a scan rate of 50 mVs^{-1}. As shown in Figure 7, CV curves exhibit typical two current peaks contributed by electro-oxidations of alcohols. Anodic peak (I_f) at around 0.87 V is attributed to oxidation currents for breaking C-H or C-C bonds during the methanol electro-oxidation in forward sweeping, while cathodic peak (I_r) at the potential of 0.66 V is assigned to oxidation currents for removing of carbonaceous residues on the Pd surface during the backward sweeping. The carbonaceous intermediates tend to strongly adsorb on the Pd surface, which can block the active
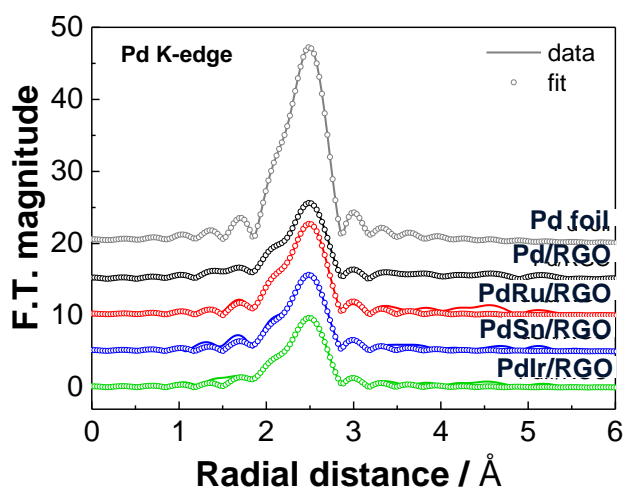
Figure 5. Fourier transforms of extended X-ray absorption fine structure (EXAFS) of Pd K-edge for Pd/RGO, PdRu/RGO, PdSn/RGO, and PdIr/RGO.

sites of catalyst for next turnover, thus making the anodic reaction more sluggish. By comparison of the characteristics of the CVs in Figure 7, addition of Ru and Sn into Pd leads to enhancements in the catalytic activity for the methanol electro-oxidation, while slight activity enhancement has been observed with the addition of Ir. The lowest onset potential and highest peak current density of methanol electro-oxidation can be observed with the PdRu/RGO catalysts, as summarized in Table 4, implying that the structural and electronic modification of Pd by the Pd-Ru interaction would highly favor the breaking of C-H bond and subsequent removal of C_1 or C_2 intermediate with the reduced activation barrier. The anodic currents normalized by the EAS values of the Pd catalyst for the methanol electro-oxidation were in order of PdRu/RGO (0.173 mAm^{-2}) > PdSn/RGO (0.143 mAm^{-2}) > PdIr/RGO (0.136 mAm^{-2}) > Pd/RGO (0.133 mAm^{-2}).
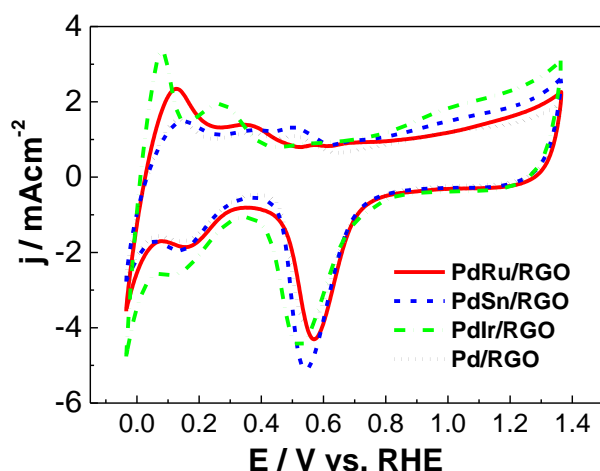

Figure 6. CVs of the Pd/RGO, PdRu/RGO, PdSn/RGO, and PdIr/RGO catalysts in 0.1 M NaOH solution at a scan rate of 50 mVs^{-1} at room temperature.
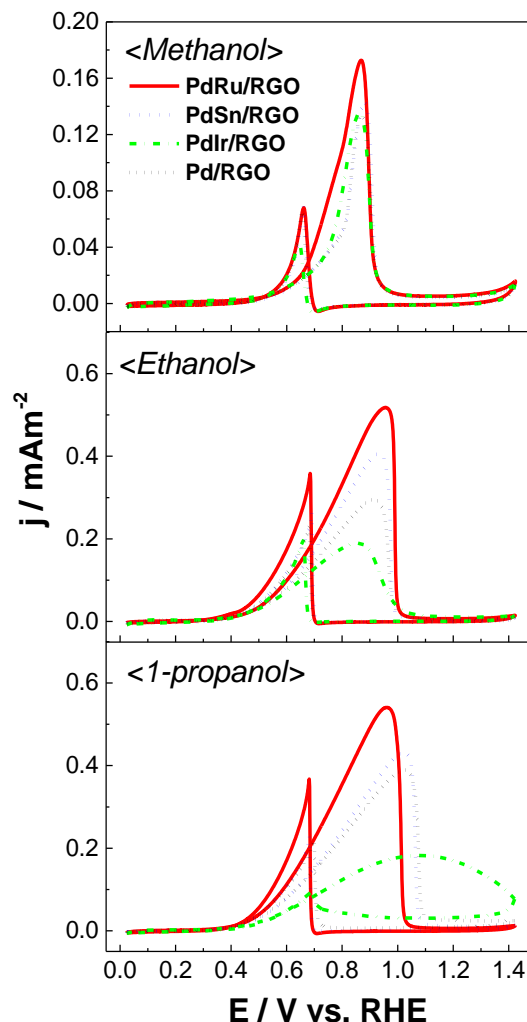

Figure 7. CVs of the Pd/RGO, PdRu/RGO, PdSn/RGO, and PdIr/RGO catalysts in 1.0 M NaOH solution containing with 1.0 M methanol, ethanol, and 1-propanol at a scan rate of 50 mVs^{-1} at room temperature.

The PdRu/RGO showed the best activity, with improvements by at least 21 % and 30 % compared with PdSn/RGO and Pd/RGO catalysts, respectively. Also, I_r/I_f ratio of the PdRu/RGO catalyst is significantly larger than that of Pd/RGO, indicating that less intermediate residues were accumulated on the catalyst during methanol electro-oxidation in the presence of ruthenium oxide.

For further investigation of ethanol and 1-propanol electro-oxidations over the prepared Pd/RGO, PdRu/RGO, PdSn/RGO, and PdIr/RGO catalysts, CVs were performed in solutions of 1.0 M NaOH with 1.0 M ethanol or 1.0 M 1-propanol in the potential range of -0.9 to 0.5 V (vs. Hg/HgO) at a scan rate of 50 mVs^{-1}. As shown in the Figure 7, the typical CV curves with the two anodic peaks for both cases of ethanol and 1-propanol were also observed during the forward and backward sweeping.

Table 4. Comparison of the electrocatalytic activities of the Pd/RGO, PdRu/RGO, PdSn/RGO, and PdIr/RGO catalysts for electro-oxidation of methanol, ethanol, and 1-propanol.

Catalysts	Electroactive surface area $(m^2 g^{-1})$	Methanol		Ethanol		1-propanol	
		E_S	I_f (mAm^{-2})	E_S	I_f (mAm^{-2})	E_S	I_f (mAm^{-2})
Pd/RGO	58	0.43	0.13	0.27	0.30	0.30	0.39
PdRu/RGO	52	0.37	0.17	0.24	0.52	0.26	0.54
PdSn/RGO	65	0.41	0.14	0.29	0.41	0.29	0.43
PdIr/RGO	62	0.25	0.14	0.25	0.19	0.32	0.18

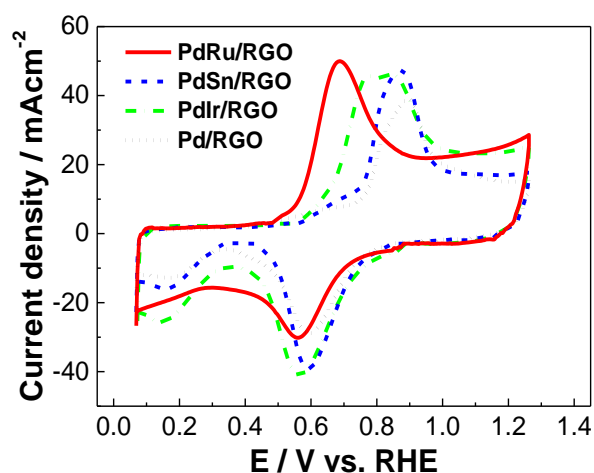I_f: Forward peak current density at 50 mVs^{-1}.
I_r: Reverse peak current density at 50 mVs^{-1}.
I_r / I_f: Ratio of reverse (I_r) to forward (I_f) peak current density.
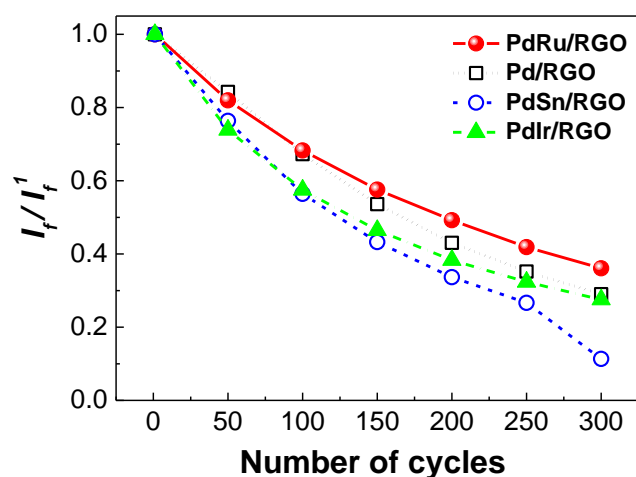E_s: Onset potential.

The onset potential in cases of the binary Pd catalysts was located at relatively lower potential than that of Pd/RGO catalyst for the electro-oxidation with ethanol and 1-propanol. The peak current densities appeared in the following order: PdRu/RGO > PdSn/RGO > Pd/RGO > PdIr/RGO. In particular, the forward peak current density of PdRu/RGO for the ethanol and 1-propanol electro-oxidation is ca. 75 % and 38 % higher than those of the Pd/RGO catalyst. The increased performance of the PdRu/RGO system toward electro-oxidations of methanol, ethanol, and 1-propanol can be rationalized as follows: Alloying of Ru with Pd changes geometric and electronic structure which can allow the effective scission of C-C and C-H bonds in the alcohol molecules. Ru species is able to adsorb oxygen containing species at lower potentials, thus residual carbonaceous species adsorbed on the catalyst could be readily oxidized by the oxidants, providing clean site for next reaction.

To understand the catalytic property with the electro-chemical oxidation of adsorbed CO on the catalyst, CO stripping voltammetry was conducted in 0.1 M NaOH solution at a sweep rate of 50 mVs^{-1}.

The electro-oxidations of the carbonaceous species and subsequent CO_{ads} oxidation process play a crucial role in alcohol electro-oxidation process. Figure 8 shows the CO stripping voltammograms of the Pd/RGO, PdRu/RGO, PdSn/RGO, and PdIr/RGO catalysts at room temperature after full adsorption of CO onto the catalyst and subsequent purging of the solution by a high purity N_2 gas. Due to the blocking of the hydrogen adsorption sites by adsorbed CO, no hydrogen adsorption peak at low potentials has been observed. The onset potentials of CO oxidation on the PdM/RGO appear to shift negatively compared to the Pd/RGO catalyst. The oxidation of an adsorbed CO molecule starts from 0.39 V by showing broad peak current with a maximum current at around 0.68 V over the PdRu/RGO catalyst, while in the case of Pd/RGO catalyst, the CO oxidation peak appears at more positive onset potential (0.42 V). This indicates that addition of Ru may induce a better ability to oxidize and remove the adsorbed CO from Pd sites by working at lower overpotentials and efficiently providing oxidant species as compared to other tested catalysts.

Figure 8. CO stripping voltammograms of the Pd/RGO, PdRu/RGO, PdSn/RGO, and PdIr/RGO catalysts in 0.1 M NaOH at a 50 mVs^{-1} scan rate at room temperature.

Figure 9. Accelerated durability test of the Pd/RGO, PdRu/RGO, PdSn/RGO, and PdIr/RGO catalysts in 1.0 M NaOH with 1.0 M methanol at a scan rate of 50 mVs^{-1} at room temperature.
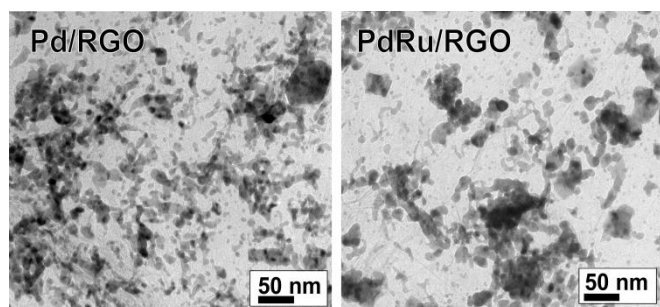
Figure 10. Representative TEM images of Pd/RGO and PdRu/RGO catalysts after electrochemical accelerated durability test in 1.0 M NaOH with 1.0 M methanol.

This PdRu/RGO catalyst also showed the improved stability in alkaline condition, as resulted in repeated CV tests in the solution of 1.0 M NaOH with 1.0 M methanol. In Figure 9, current profiles with the repeated cycles for the methanol electro-oxidation were plotted up to 300 cycles. The forward peak current (I_f) measured at the corresponding cycle of the CVs was divided by the highest current (I_f^1) with the fully activated cycle during the reaction. The PdRu/RGO catalyst displayed higher I_f/I_f^1 values with cycle number. The activity loss of Pd/RGO at 300th cycle was approximately 70 % of that in the fully activated first cycle, whereas the PdRu/RGO catalyst revealed the much retarded activity loss from the initial activity. As shown in the Figure 10, the Pd/RGO and PdRu/RGO revealed particle growth after the cycle tests when compared with Figure 1 for the fresh catalysts, suggesting a possible reason for the deactivation of Pd-based nanoparticle catalysts, which might be resulted from the dissolution, redeposition and coalescene of Pd during cycling test.[49]

Figure 11 compares the electrocatalytic activity obtained from the forward peak current density in the CVs (in Figure 7) as the function of the second metal elements. It can be seen that the PdRu/RGO catalyst resulted in remarkably enhanced electrocatalytic activity in terms of maximum forward peak current densities in all electro-oxidation cases with methanol, ethanol, and 1-propanol. This observation indicates that the metal oxide such as ruthenium oxide contributes to improving the activity of alcohol oxidation over the Pd/RGO and facilitating the oxidative desorption of the intermediate products. In addition, electronic interaction between Ru and Pd might influence to high anti-poisoning capability through weakening the bond between CO and Pd metal.

Conclusion

In this report, electro-oxidations of methanol, ethanol, and 1-propanol were carried out over the PdRu/RGO, PdSn/RGO, PdIr/RGO, and Pd/RGO catalysts. Even with high amount of metal loadings up to 60 wt. %, highly dispersed catalytic nanoparticles were effectively prepared on the RGO. Electrochemical tests revealed that the Pd-based binary catalysts showed the higher electrocatalytic performances for the electro-oxidations of primary alcohols (methanol, ethanol, and 1-propanol) in the alkaline condition. The PdRu/RGO

catalyst performed well with significantly improved specific activities of 30 %, 75 %, and 38 % for the electro-oxidations of methanol, ethanol, and 1-propanol, respectively, as compared to Pd/RGO. This improved activity can be rationalized by the structural and electronic modifications, such as changes in lattice parameter, oxidation state of PdM over the RGO catalyst and charge transfer from Ru to Pd with modification of the Pd d-band states which can beneficially affect the activity of the binary catalyst by facilitating the C-C bond scission and increasing the tolerance over poisoning by CO or CO-like residues. Also, the synergistic effect of Ru on PdRu/RGO catalyst could help complete oxidation of CO or CO-like species on Pd sites and make the catalytic sites free for methanol, ethanol, and 1-propanol electro-oxidation, thus leading to improvements of electrocatalytic activity and stability.
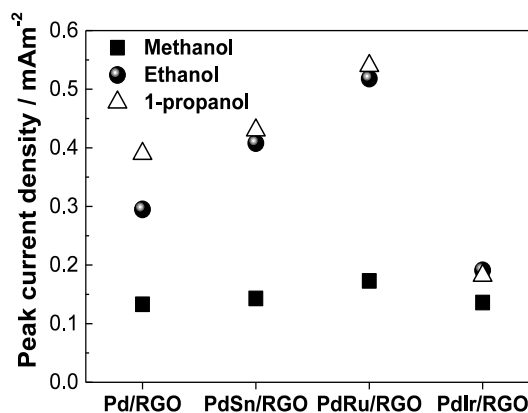

Figure 11. The electrocatalytic activity comparison of prepared catalysts for methanol, ethanol, and 1-propanol.

Author Information

Corresponding author
*E-mail: wbkim@gist.ac.kr

Notes and references

[a]*School of Materials Science and Engineering, Gwangju Institute of Science and Technology (GIST), Gwangju, 500-712, Republic of Korea. E-mail: wbkim@gist.ac.kr; Fax: +82 62 7152304; Tel: +82 62 7152317*
[b]*Research Institute for Solar and Sustainable Energies (RISE), Gwangju Institute of Science and Technology (GIST), Gwangju, 500-712, Republic of Korea*
[c]*Surface Technology Division, Korea Institute of Materials Science (KIMS), Changwon 641-010, Republic of Korea*

^{d}Department of Physics and Photon Science, Gwangju Institute of Science and Technology (GIST), Gwangju, 500-712, Republic of Korea

1   C. Lamy, A. Lima, V. Lerhen, F. Delime, C. Coutanceau, J. -M. Léger, *J. Power Sources,* 2002, **105**, 283.

2   C. Bianchini, P. K. Shen, *Chem. Rev.,* 2009, **109**, 4183.

3   V. Bambagioni, C. Bianchini, A. Marchionni, J. Filippi, F.Vizza, J. Teddy, P. Serp, M. Zhiani, *J. Power Sources,* 2009, **190**, 241.

4   S. G. Chalk, J. F. Miller, *J Power Sources,* 2006, **159**, 73.

5   K. Geissler, E. Newson, F. Vogel, T. -B. Truong, P. Hottinger, A. Wokaun, *Phys. Chem. Chem. Phys*., 2001, **3**, 289.

6   J. H. Kim, S. M. Choi, S. H. Nam, M. H. Seo, S. H. Choi, W. B. Kim, *Appl. Catal. B-Environ.,* 2008, **82**, 89.

7   A. V. Tripković, K. D. Popović, J. D. Lović, *Electochim. Acta,* 2001, **46**, 3163.

8   L. Carrette, K. A. Friedrich, U. Stimming, *Fuel Cells,* 2001, **1**, 5.

9   C. Lamy, E. M. Belgsir, J. -M. Léger, *J. Appl. Electrochem*., 2001, **31**, 799.

10   B. Y. Xia, H. B. Wu, X. Wang, X. W. Lou, *J. Am. Chem. Soc*., 2012, **134**, **13934.**

11   B. Y. Xia, W. T. Ng, H. B. Wu, X. Wang, X. W. Lou, *Angew. Chem. Int. Ed.,* 2012, **51**, 7213.

12   G. Gui, S. Song, P. K. Shen, A. Kowal, C. Bianchini, *J. Phys. Chem. C,* 2009, **113**, 15639.

13   L. Ma, D. Chu, R. Chen, *Int. J. Hydrog. Energy,* 2012, **37**, 11185.

14   M. Baldauf, D. M. Kolb, *J. Phys. Chem,* 1996, **100**, 11357.

15   R. S. Amin, R. M. A. Hameed, K. M. El-Khatib, M. E. Youssef, A. A. Elzatahry, *Electrochim. Acta,* 2012, **59**, 499.

16   C. Xu, Z. Tian, P. Shen, S. P. Jiang, *Electrochim. Acta,* 2008, **53**, 2610.

17   A. Ruban, B. Hammer, P. Stoltze, H. L. Skriver, J. K. Norskov, *J. Mol. Catal. A Chem.,* 1997, **115**, 421.

18   J. Greeley, J. K. Norskov, M. Mavrikakis, *Annu. Rev. Phys. Chem.,* 2002, **53**, 319.

19   Y. Y. Tong, C. Rice, A. Wieckowski, and E. Oldfield, *J. Am. Chem. Soc.,* 2000, **122**, 1123.

20   M. Watanabe, S. Motoo, *J. Electroanal. Chem*., 1975, **60**, 267.

21   M. Watanabe, S. Motoo, *J. Electroanal. Chem*., 1975, **60**, 275.

22   P. -C. Su, H. -S. Chen, T. -Y. Chen, C. -W. Liu, C. -H. Lee, J. -F. Lee, T. -S. Chan, K. -W. Wang, *Int. J. Hydrog. Energy,* 2013, 38, 4474.

23   L. Y. Chen, N. Chen, Y. Hou, Z. C. Wang, S. H. Lv, T. Fujita, J. H. Jian, A. Hirata, M. W. Chen, *ACS Catal.*, 2013, **3**, 1220.

24   M. H. Seo, S. M. Choi, J. K. Seo, S. H. Noh, W. B. Kim, B. Han, *Appl. Catal. B-Environ.,* 2013, **129**, 163.

25   Y. Wang, T. S. Nguyen, X. Liu, X. Wang, *J. Power Sources,* 2010, **195**, 2619.

26   S. T. Nguyen, H. M. Law, H. T. Nguyen, N. Kristian, S. Wang, S. H. Chan, X. Wang, *Appl. Catal. B-Environ.,* 2009, **91**, 507.

27   A. Peigney, C. Laurent, E. Flahaut, R. R. Bacsa, A. Rousset, *Carbon,* 2001, **39**, 507.

28   B. F. Machado, P. Serp, *Catal. Sci. Technol.,* 2012, **2**, 54.

29   Z. -S. Wu, W. Ren, L. Gao, J. Zhao, Z. Chen, B. Liu, D. Tang, B. Yu, C. Jiang, H. -M. Cheng, *ACS Nano,* 2009, **3**, 411.

30   S. M. Choi, M. H. Seo, H. J. Kim, W. B. Kim, *Synth. Mat.,* 2011, **161**, 2405.

31   W. S. Hummers, R. E. Offeman, *J. Am. Chem. Soc*., 1958, **80**, 1339.

32   C. D. Wagner, L. E. Davis, M. V. Zeller, J. A. Taylor, R. H. Raymond, L. H. Gale, *Sulf. Interface Anal*., 1981, **3**, 211.

33   B. Ravel and M. Newville, *J. Synchrotron Rad*., 2005, **12**, 537.

34   A. F. Well, Structural Inorganic Chemistry, 5th ed., Claredon, Oxford, 1984.

35   S. Mao, Z. Wen, T. Huang, Y. Hou, J. Chen, *Energy Environ. Sci.,* 2014, 7, 609.

36   V. Radmilovi´, H. A. Gasteiger, P. N. Ross Jr., *J. Catal.,* 1995, **154**, 98.

37   N. Krishnankutty, M. A. Vannice, *J. Catal*., 1995, **155**, 312.

38   L. Ma, H. He, A. Hsu, R. Chen, *J. Power Sources,* 2013, **241**, 696.

39   W. Zhang, R. Wang, H. Wang, Z. Lei, *Fuel Cells,* 2010, **10**, 734.

40   U. B. Demirci, *J. Power Sources,* 2007, **173**, 11.

41   R. K. Raman, A. K. Shukla, A. Gayen, M. S. Hegde, K. R. Priolkar, P. R. Sarode, S. Emura, *J. Power Sources,* 2006, **157**, 45.

42   Y. Liang, H. Zhang, H. Zhong, X. Zhu, Z. Tian, D. Xu, B. Yi, *J. Catal*., 2006, **238**, 468.

43   A. I. Frenkel, C. W. Hills, R. G. Nuzzo, *J. Phys. Chem. B*., 2001, **105**, 12689.

44   W. Vielstich, A. Lamm, H. A. Gasteiger, Handbook of Fuel Cells, John Wiley & Sons, England, 2003.

45   Y. Kim, Y. Noh, E. J. Lim, S. Lee, S. M. Choi, W. B. Kim, *J. Mater. Chem. A,* 2014, **2**, 6976.

46   W. B. Kim, E. D. Park, C. W. Lee, J. S. Lee, *J. Catal*., 2003, **218**, 334.

47   L. Jiang, A. Hsu, D. Chu, R. Chen, *J. Electrochem. Soc*., 2009, **156**, B643.

48   T. Chierchie, C. Mayer, W. J. Lorenz, *J. Electroanal. Chem*., 1982, **135**, 211.

49   M. H. Seo, E. J. Lim, S. M. Choi, S. H. Nam, H. J. Kim, W. B. Kim, *Int. J. Hydrog. Energy,* 2011, 36, 11545.